Hirvi, Pauliina; Nissilä, Ilkka; Maria, Ambika; Fang, Qianqian; Kotilahti, Kalle; Heiskala, Juha; Tuulari, Jetro J.; Karlsson, Linnea; Hannukainen, Antti; Karlsson, Hasse; Hyvönen, Nuutti

Improved utilization of frequency-domain data for optical tomographic imaging of the human brain

Published in:
Optical Tomography and Spectroscopy of Tissue XV

DOI:
10.1117/12.2649042

Published: 01/01/2023

Document Version
Publisher's PDF, also known as Version of record

Improved utilization of frequency-domain data for optical tomographic imaging of the human brain

Pauliina Hirvi, Ilkka Nissilä, Ambika Maria, Qianqian Fang, Kalle Kotilahti, et al.

Pauliina Hirvi, Ilkka Nissilä, Ambika Maria, Qianqian Fang, Kalle Kotilahti, Juha Heiskala, Jetro J. Tuulari, Linnea Karlsson, Antti Hannukainen, Hasse Karlsson, Nuutti Hyvönen, "Improved utilization of frequency-domain data for optical tomographic imaging of the human brain," Proc. SPIE 12376, Optical Tomography and Spectroscopy of Tissue XV, 123760A (7 March 2023); doi: 10.1117/12.2649042

SPIE.

Event: SPIE BiOS, 2023, San Francisco, California, United States

Improved utilization of frequency-domain data for optical tomographic imaging of the human brain

Pauliina Hirvi[a], Ilkka Nissilä[b], Ambika Maria[c,d], Qianqian Fang[e], Kalle Kotilahti[b,d], Juha Heiskala[f], Jetro J. Tuulari[c,d,g], Linnea Karlsson[d,h,i], Antti Hannukainen[a], Hasse Karlsson[c,d], and Nuutti Hyvönen[a]

[a]Aalto University, Department of Mathematics and Systems Analysis, P.O. Box 11100, FI-00076 AALTO, Espoo, Finland
[b]Aalto University, Department of Neuroscience and Biomedical Engineering, P.O. Box 12200, FI-00076 AALTO, Espoo, Finland
[c]University of Turku and Turku University Hospital, Department of Psychiatry, FI-20014 Turun yliopisto, Turku, Finland
[d]FinnBrain Birth Cohort Study, Turku Brain and Mind Center, Department of Clinical Medicine, University of Turku, Turku, Finland
[e]Northeastern University, Department of Bioengineering, 360 Huntington Ave, Boston, MA 02115, USA
[f]HUS Medical Imaging Center, Department of Clinical Neurophysiology, Helsinki University Hospital and University of Helsinki, Helsinki, Finland
[g]Turku Collegium for Science and Medicine and Technology, University of Turku, Turku, Finland
[h]University of Turku and Turku University Hospital, Department of Paediatrics and Adolescent Medicine, Finland
[i]Centre for Population Health Research, Turku University Hospital and University of Turku, Turku, Finland

ABSTRACT

Frequency-domain (FD) optical tomography instruments modulate the intensity of the light source at a radio frequency and measure the amplitude and phase shift of the detected photon density wave. The differing spatial sensitivities of amplitude and phase to the optical properties of tissue suggest that inclusion of phase data can improve the image reconstruction accuracy. This study describes our methodology for improved use of FD data in conjunction with a Monte Carlo (MC) forward solver (Monte Carlo eXtreme; MCX) and a voxel-based model of a two-year-old child's head. The child participated our previous study where subjects were stimulated with affective (slow brushing) and non-affective touch (fast brushing) to their right forearm, and the responses were measured from the left hemisphere with our in-house 16-channel high-density FD system. We implemented the computation of the FD sensitivity profiles to the MCX photon simulation software, and validated the output against our in-house MC code. We used simulated and the real experimental touch response data to observe the effects of including both FD data types to the image reconstruction instead of amplitude data alone. For the simulated and experimental case, we observed that the inclusion of phase data increases the reconstructed contrast in the brain. The individual touch responses showed similarity to the group-level results in our original publication with 16 subjects and amplitude data alone, and other literature.

Keywords: Affective touch, Atlas model, Diffuse optical tomography, Frequency-domain, Image reconstruction, Monte Carlo, Regularization, Toddler brain

Further author information: (Send correspondence to P.H.)
P.H.: E-mail: pauliina.hirvi@aalto.fi, Telephone: +358 400 635598

Optical Tomography and Spectroscopy of Tissue XV, edited by Sergio Fantini, Paola Taroni, Proc. of SPIE Vol. 12376, 123760A · © 2023 SPIE
1605-7422 · doi: 10.1117/12.2649042

1. INTRODUCTION

Diffuse optical tomography (DOT) is a functional imaging method where tissue is illuminated with red and/or near-infrared light (630–950 nm) to obtain three-dimensional maps of haemodynamic changes.[1,2] DOT has gained increasing interest as a relatively light-equipped and inexpensive alternative for imaging human brain activity. DOT is suitable for subjects of all ages, but particularly attractive for imaging children.[3–5] The convenient setup and relatively good tolerance to subject movement make it feasible to image awake toddlers which can be difficult using other methods.

DOT instruments are classified into continuous-wave (CW), time-domain (TD) and frequency-domain (FD) based on their measurement principle. CW is the most common, but only TD and FD provide time-resolved information that is required for estimating the tissue-specific absorption and scattering coefficients. FD instruments produce intensity-modulated light in the radio-frequency range and measure the amplitude and phase shift of the detected photon density wave.

In this paper, we introduce our algorithm for image reconstruction based on both FD data types and compare the results to images reconstructed from amplitude data alone. The DOT image reconstruction requires solving a highly ill-posed and underdetermined inverse problem where the number of measurements is typically much lower than the number of unknown model elements. Doubling the number of measurements by adding another data type should aid in solving the inverse problem, especially since the two data types have different spatial sensitivities in the imaged domain. Doulgerakis *et al.* (2019) observed the improved image quality in simulations with 24 adult models and one real measurement example, using the finite element method to solve the diffusion approximation of the Radiative Transfer Equation (RTE) as the forward model.[6] We use the Monte Carlo (MC) forward solver as it can more easily accommodate low-scattering cerebrospinal fluid (CSF) regions.

We used the model and data for a two-year-old subject from our recent publication by Maria *et al.* (2022).[7] In that paper, we imaged responses to slow and fast brushing of the right forearm in 16 two-year-old children whose families participated the FinnBrain Birth Cohort Study.[8] The experimental data was acquired with the intensity-modulated DOT system built at Aalto University[9] by placing a high-density (HD) measurement probe over the left frontotemporal brain region. The data analysis pipeline includes estimating the baseline optical parameters, averaging the amplitude and phase responses, computing the sensitivity profiles, and optimizing the reconstruction algorithm.

2. METHODS

In the current framework, the forward problem of DOT means estimating the FD measurements at the detectors for a known head model, optical parameters and optode locations. The RTE gives the most accurate description of the distribution of light within tissue, but is generally too complex to solve in a realistic head geometry. Instead, we used stochastic Monte Carlo (MC) methods and simulate the propagation of billions of photons to estimate the probability distribution of the trajectories of the detected photons.

2.1 Forward Model and Sensitivity Profiles

As the MC forward solver, we used the MATLAB (MathWorks, Natick, MA, USA) interface of the Monte Carlo eXtreme (MCX; www.mcx.space) software for voxel (3D pixel)-based media domain models.[10] Using the recorded photon trajectories, the relative magnitude of the measured complex intensity ($I = X + \mathrm{i}Y$) can be estimated as the sum of the final weights w_p of the detected photon packets p as[11]

$$|I| = \sum_p w_p = \sum_p \exp(-\sum_v \mu_{a,v}\, l_{p,v})\,,$$

where $l_{p,v}$ is the path length of photon p in voxel v, and $\mu_{a,v}$ is the absorption coefficient of voxel v. The final weights are computed according to exponential attenuation assuming initial weight of 1 for each packet. The

corresponding real (X) and imaginary (Y) components can be computed as[12]

$$\begin{cases} I_{\mathrm{Re}} = X = \sum_p \left[w_p \cos\left(2\pi f t_p\right) \right], \\ I_{\mathrm{Im}} = Y = \sum_p \left[w_p \sin\left(2\pi f t_p\right) \right], \end{cases} \tag{1}$$

where f is the modulation frequency of the instrument, and t_p is the total time-of-flight of the photon p from launch to detection, which can be computed by multiplying the total path length with n/c, where n is the refractive index and c is the speed of light in vacuum. The FD amplitude (A) and phase shift (φ) estimates can be computed from the previous as[12]

$$\begin{cases} A = \sqrt{X^2 + Y^2}, \\ \varphi = \mathrm{atan2}\left(\dfrac{Y}{X}\right). \end{cases} \tag{2}$$

The elements of the Jacobian matrices J, or the Fréchet derivatives for X and Y with respect to the voxel-wise absorption coefficients can be derived to be[12,13]

$$\begin{cases} J_X(v) = \dfrac{\partial X}{\partial \mu_{a,v}} = \sum_p \left[\dfrac{\partial w_p}{\partial \mu_{a,v}} \cos\left(2\pi f t_p\right) \right] = -\sum_p \left[l_{p,v}\, w_p \cos\left(2\pi f t_p\right) \right], \\ J_Y(v) = \dfrac{\partial Y}{\partial \mu_{a,v}} = \sum_p \left[\dfrac{\partial w_p}{\partial \mu_{a,v}} \sin\left(2\pi f t_p\right) \right] = -\sum_p \left[l_{p,v}\, w_p \sin\left(2\pi f t_p\right) \right], \end{cases}$$

since MCX implements the microscopic Beer Lambert law and the trajectories of the photons (nor t_p) do not depend on $\mu_{a,v}$. These give the sensitivity profiles for the measurements, which for the FD amplitude (A), log-amplitude and phase shift (φ) can be computed as

$$\begin{cases} J_A(v) = \dfrac{\partial A}{\partial \mu_{a,v}} = \dfrac{1}{A}\left(X \dfrac{\partial X}{\partial \mu_{a,v}} + Y \dfrac{\partial Y}{\partial \mu_{a,v}} \right), \\ J_{\log A}(v) = \dfrac{\partial \log A}{\partial \mu_{a,v}} = \dfrac{1}{A^2}\left(X \dfrac{\partial X}{\partial \mu_{a,v}} + Y \dfrac{\partial Y}{\partial \mu_{a,v}} \right), \\ J_\varphi(v) = \dfrac{\partial \varphi}{\partial \mu_{a,v}} = \dfrac{1}{A^2}\left(X \dfrac{\partial Y}{\partial \mu_{a,v}} - Y \dfrac{\partial X}{\partial \mu_{a,v}} \right). \end{cases} \tag{3}$$

The computation of the J_X and J_Y Jacobians was included to the MCX "replay" feature.[14] The J_A and J_φ Jacobians can be computed from these using tissue-wise partial path lengths with Eqs. (1), (2) and (3).

Finally, we note that for validation purposes, the difference quotient (DQ) or finite perturbation estimates for the Jacobians can be computed as

$$\begin{cases} J_A(v) \approx \dfrac{\Delta A}{\Delta \mu_{a,v}}, \\ J_\varphi(v) \approx \dfrac{\Delta \varphi}{\Delta \mu_{a,v}}, \end{cases} \tag{4}$$

by setting $\Delta\mu_{a,v}$ as a sufficiently small perturbation from the baseline value, and simulating the measurement estimates before and after the perturbation.

2.2 Image Reconstruction and Regularization

The Jacobian matrices $J((s,d),v)$, where each row corresponds to one source (s) – detector (d) pair, can be used to approximate a linear relationship between the changes in the measurements (difference imaging) and the changes in the tissue absorption as $\Delta \log \vec{A} \approx J_{\log A} \Delta\vec{\mu}_a$ and $\Delta\vec{\varphi} \approx J_\varphi \Delta\vec{\mu}_a$, where $\Delta\vec{\mu}_a$ is a vector with the voxel-wise absorption changes in the field-of-view (FOV). Thus, the inverse problem of image reconstruction can be formulated as[11,13]

$$\min_{\Delta\vec{\mu}_a} \big(\alpha|\Delta \log \vec{A} - J_{\log A}\Delta\vec{\mu}_a|^2 + \beta|\Delta\vec{\varphi} - J_\varphi\Delta\vec{\mu}_a|^2 + \gamma|\Delta\vec{\mu}_a|^2 + \delta|L_{tt}\Delta\vec{\mu}_a|^2\big), \tag{5}$$

where the last two terms implement norm minimizing and second-order smoothening Tikhonov regularization. The tissue-specific Laplacian matrix L_{tt}, which corresponds to the negative Laplace operator, is defined component-wise as

$$L_{tt}(i,j) = \begin{cases} \mathrm{NN}(i) & \text{if } i = j\,, \\ -1 & \text{if } i \text{ and } j \text{ are neighbors of same tissue type}\,, \\ 0 & \text{else}\,, \end{cases}$$

where $\mathrm{NN}(i)$ is the number of neighbors of same tissue type in the 6-neighborhood of voxel i. In particular, L_{tt} does not spread activity over tissue boundaries. We select the positive weights α and β so that both data terms in (5) have initial weight of 1, and the regularization parameters γ and δ are selected empirically. If we only use log-amplitude data, the weight α is multiplied by 2.[11]

If we combine the weighted measurements into one longer vector $\vec{M}_w = [\sqrt{\alpha}\ \log\vec{A};\ \sqrt{\beta}\ \vec{\varphi}]$ and mark the corresponding piled weighted Jacobians as J_w, along with $I_w = \sqrt{\gamma}\ I$ and $L_w = \sqrt{\delta}\ L_{tt}$, the problem in (5) simplifies to

$$\min_{\Delta\vec{\mu}_a} \big(|\Delta\vec{M}_w - J_w\Delta\vec{\mu}_a|^2 + |I_w\Delta\vec{\mu}_a|^2 + |L_w\Delta\vec{\mu}_a|^2\big).$$

The solution of this, originally underdetermined but regularized, minimization problem can be written as

$$\Delta\vec{\mu}_a = \big(J_w^{\mathrm{T}}J_w + \underbrace{(I_w^{\mathrm{T}}I_w + L_w^{\mathrm{T}}L_w)}_{\text{sparse}}\big)^{-1} J_w^{\mathrm{T}}\Delta\vec{M}_w\,.$$

Since J_w is full and typically very wide ($366 \times (2.2 \times 10^5)$ in this study), directly operating with the inverse of the matrix within the brackets is computationally very expensive. However, the sparse matrix $I_w^{\mathrm{T}}I_w + L_w^{\mathrm{T}}L_w$ is positive definite (when $\gamma > 0$) and its inverse can be efficiently obtained from its Cholesky decomposition. The whole inverse problem can be solved efficiently by combining the Cholesky decomposition with the Woodbury matrix identity to get

$$\begin{cases} V = (I_w^{\mathrm{T}}I_w + L_w^{\mathrm{T}}L_w)^{-1}\,, \\ \Delta\vec{\mu}_a = \big(V - VJ_w^{\mathrm{T}}(I + J_wVJ_w^{\mathrm{T}})^{-1}J_wV\big)J_w^{\mathrm{T}}\Delta\vec{M}_w\,, \end{cases}$$

where operating with the remaining inverse matrix is performed using MATLAB's backslash-operator without explicitly inverting the matrix. Note that the dimension of the square matrix $I + J_wVJ_w^{\mathrm{T}}$ (where I is the identity matrix) is the same as the number of measurement data, i.e., very small compared to the width of J_w.

The 3D haemodynamic activity maps, or voxel-wise changes in the total haemoglobin concentration (HbT), can be obtained from the $\Delta\vec{\mu}_a$-map with the conversion

$$\Delta\vec{\mathrm{HbT}} = \frac{\log_{10}(e)}{\alpha_{\mathrm{HbT}}} \times \Delta\vec{\mu_a}, \tag{6}$$

where $\alpha_{\mathrm{HbT}} = 0.08524\,\mathrm{mM}^{-1}\,\mathrm{mm}^{-1}$ is the extinction coefficient at a wavelength of 798 nm.[15] Scattering changes related to neuronal activity are assumed to be small and thus are not considered in the reconstruction.

3. IMPLEMENTATION

For this study, we selected two subjects from the previous touch study by Maria *et al.* (2022):[7] The main subject (Subject 1) was used for the image reconstructions from real experimental data since the probe placement was optimal for the considered regions. The second subject's (Subject 2) head model was used to observe the FD Jacobians.

3.1 Models

The model generation process was described in detail by Hirvi (2019)[16] and Maria *et al.* (2022).[7] Shortly, the individual voxel-based head models for each child were obtained by deforming the population-level atlas by Shi *et al.* (2011)[17] to match the exterior geometry of the subject's head. The exterior shape and optode positions were reconstructed with photogrammetry. In all cases presented in Sec. 4, we simulated 2×10^9–10^{10} photon packets per source of the collimated Gaussian beam type. The beam waist radius was 1.25 mm, and the detector radius was 1.82 mm. The voxel side length in the models was 1 mm.

An axial slice of the segmented anatomy for Subject 2 is shown in Fig. 2B. The tissue types include combined scalp and skull (S&S), grey matter (GM), white matter (WM), and two separate CSF compartments; a semi-diffusive subarachnoid layer (CSF-1) and more transparent low-scattering CSF in the sulci and ventricles (CSF-2). The optical parameters selected for each tissue type are given in Tab. 1. The baseline absorption and scattering coefficients for S&S and GM were estimated by fitting simulated data to coupling error and baseline drift corrected calibrated amplitude and phase shift measurements, as described in Maria *et al.* (2022).[7] This approach was chosen since we did not find literature-based values for two-year-olds and values in general vary across studies and are often from *in vitro* samples. For this study, we increased the CSF-2 scattering to $0.3\,\mathrm{mm}^{-1}$, to model the possible arachnoid trabeculae and veins that extend to the sulci. Modeling light propagation in the cerebrospinal fluid (CSF) is presumably important especially when imaging functional areas in the sulci.

Table 1. Tissue-specific optical parameters.[7]

Tissue type	$\mu_a\,[\mathrm{mm}^{-1}]$	$\mu_s\,[\mathrm{mm}^{-1}]$	g	n
Scalp & Skull	0.0120	8	0.9	1.35
CSF-1	0.0040	3	0.9	1.35
CSF-2	0.0020	0.3	0.9	1.35
GM	0.0140	22	0.9	1.35
WM	0.0032	84	0.9	1.35

3.2 Measurements

The in-house (Aalto University) 16-channel FD system[9] was equipped with a silicone-based, flexible, high-density fibreoptic probe with 15 sources and detectors, and microelectromechanical systems (MEMS) switches to facilitate faster imaging. The FD instrument measures the amplitude and phase shift of the detected photon density wave for a broad range of source–detector separations (6–60 mm), facilitating the estimation of the baseline absorption and scattering parameters, and providing a richer set of spatial sensitivity profiles for image reconstruction. For the two-year-olds, we selected a single wavelength of 798 nm. The instrument was intensity-modulated at 100 MHz.

During the experiments, the two-year-old sat on their parent's lap in a dimmed room, as described by Maria *et al.* (2022).[7] Slow brushing (affective touch) was applied with a soft paint brush at a brushing speed of 3 cm/s, and fast brushing (non-affective touch) at speed 30 cm/s. Coauthor AM brushed the right forearm of the child, and the responses were measured contralaterally over the left frontotemporal brain regions.

The time courses of the responses to slow and fast brushing were resolved explicitly from the filtered raw signal via finite impulse response (FIR) deconvolution. Absolute data calibration was described in Ref.[9] with the exception that the inter-channel differences were determined using a homogeneous tissue-equivalent cylinder with one fiber (either source 1 or detector 2) placed in the center.

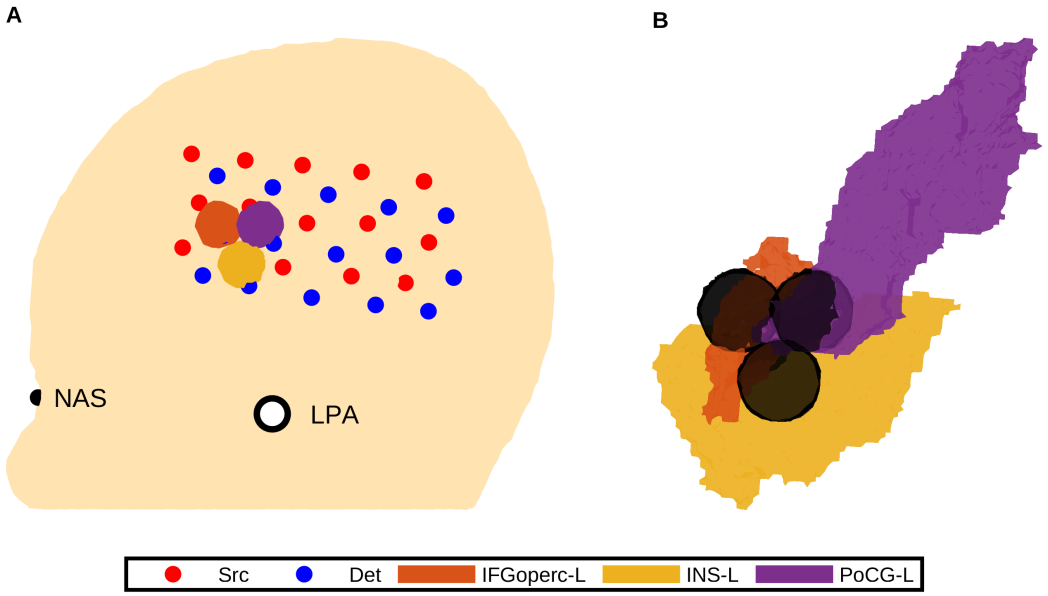

Figure 1. Visualizations of cylinders drilled from the head surface towards the three selected Regions of Interest (ROI) on the left hemisphere. The drilling direction points from the left (LPA) to the right (RPA) preauricular point, and the radius of each cylinder is 8 mm and depth 25 mm. A: Head surface with the cylinders, sources (Src) and detectors (Det). B: The three ROIs and the corresponding cylinders in black. (**Subject 1**)

3.3 Region of Interest Analysis

We selected the left opercular inferior frontal gyrus (IFGoperc-L), the left insular cortex (INS-L) and the left postcentral gyrus (PoCG-L) as our three regions of interest (ROI) where we observed the reconstructed HbT changes for slow and fast brushing stimuli. Fig. 1A–B visualize the ROIs and their approximate locations. In Maria *et al.* (2022), the INS-L ROI showed statistically significantly greater responses to slow versus fast brushing on the group level, and a cluster in the inferior PoCG-L showed greater responses to fast versus slow brushing.[7]

We observed the temporal maximum, minimum and mean HbT changes over each ROI. In addition, we observe the mean responses over 1 mm-thick disk-intersections of 8 mm-radius cylinders drilled from the head surface towards the center of the ROI along an axis pointing from the left preauricular point (LPA) towards the right preauricular point (RPA). For the PoCG-L ROI, instead of its geometric center we used the approximate location of the cluster in Maria *et al.* (2022), which is near the inferior tip of the PoCG-L and includes voxels in the Rolandic operculum (ROL-L).[7] Fig. 1A shows the locations of the cylinders for each ROI on the left hemisphere, and Fig. 1B visualizes the coverage of the ROI by the corresponding cylinder. We note that the cylinders only observe a partial intersection of each ROI, but provide a tool for observing the behaviour of the reconstructions at different depths from the surface of the head.

4. RESULTS

4.1 Validation of FD Jacobians

Figs. 2C–H compare axial slices of the amplitude (Fig. 2C, E, G) and phase shift (Fig. 2D, F, H) Jacobians according to the novel MCX "rf replay" feature included to the original " replay" feature[14] (Fig. 2C-D), the difference quotient estimates (Fig. 2E–F), and an in-house MC algorithm (Fig. 2G–H) (coauthor IN). Fig. 2A visualizes the locations of the selected source 1 – detector 2 pair on the left hemisphere. The axial slice ($x = 69$) is halfway between the optodes, and the segmented anatomy is shown in Fig. 2B. The difference quotient Jacobian estimates were computed with Eq. (4) by setting $\Delta\mu_{a,v}$ as a 5% increase in the voxel's baseline absorption value. The Jacobian values were normalized with their respective absolute maximum value in the slice, reported as "NF" (Normalization Factor) for each subfigure.

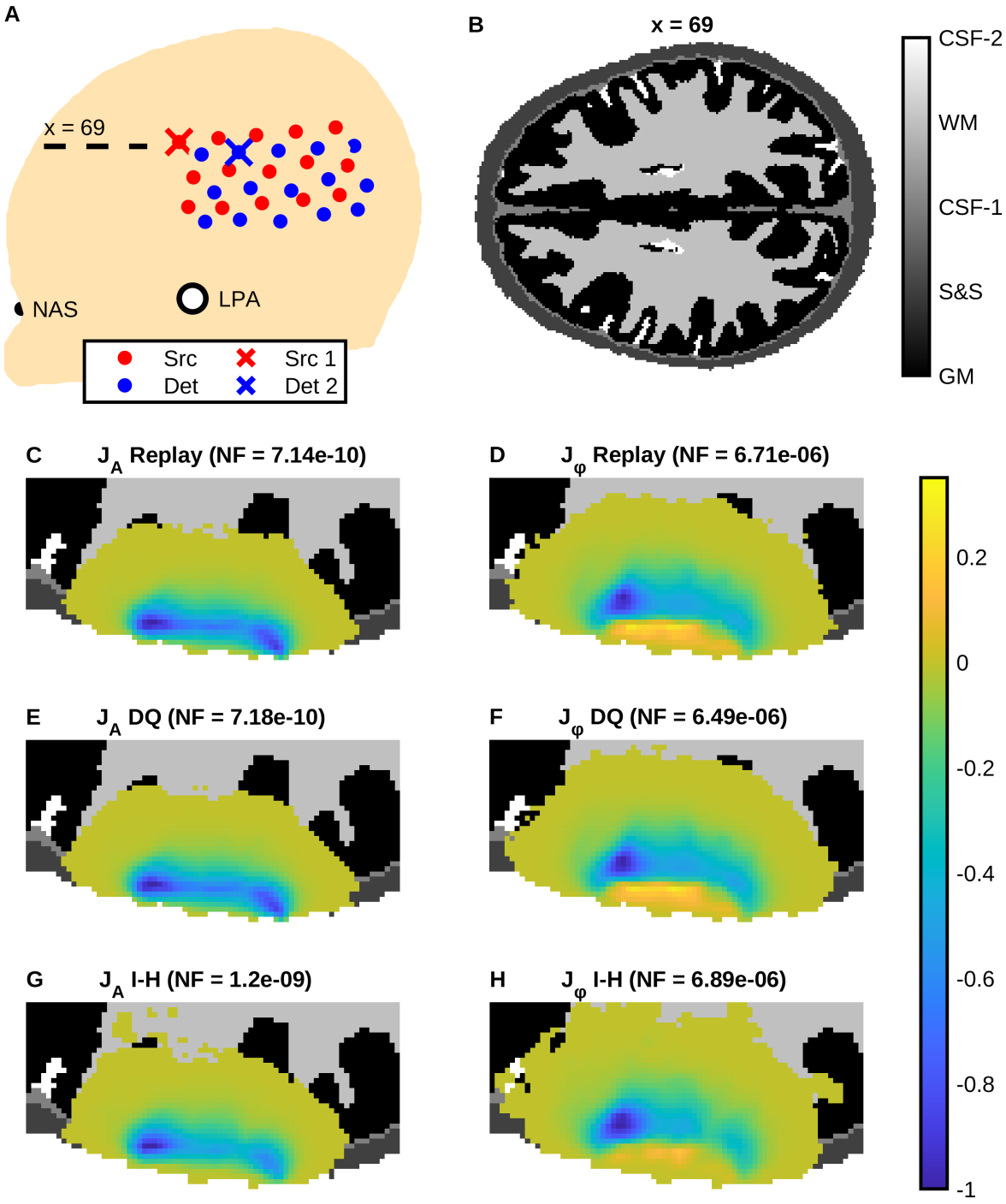

Figure 2. Comparison of the amplitude and phase shift Jacobians for source 1 and detector 2 (A), in a nearly axial slice $x = 69$ halfway between the optodes (B), according to three different algorithms: C–D: MCX "rf replay", E–F: MCX difference quotient (DQ)/finite perturbation estimates, G–H: In-house MC code. The values in each slice were normalized with their maximum absolute value "NF" (Normalization Factor). NAS = nasion, GM = grey matter, S&S = scalp and skull, CSF = cerebrospinal fluid, WM = white matter. (**Subject 2**)

The MCX "rf replay" Jacobians and the difference quotient estimates match very well. The phase Jacobians match well across all three algorithms, but there is some variation in the peak amplitude sensitivities according to our in-house algorithm. These relate at least partly to the facts that the in-house Jacobians were computed in 2 mm-resolution with fewer (10^8) photon packets. In addition, the in-house algorithm has been programmed independently of the MCX software and, for example, the source models differ. Nevertheless, these results show sufficient similarity supporting the validity of the new "rf replay" feature.

The observed spatial differences in Fig. 2 highlight the potential benefit of using both data types to aid the ill-posed image reconstruction, in particular, for differentiating between extracerebral physiology in the scalp and neurovascular responses in the gray matter of the brain.

4.2 Image Reconstruction

For all the following reconstructions from simulated and real measured human data, we set the regularization weights γ and δ in Eq. (5) to 0.05. In cases where only log-amplitude data is used, its weight is doubled. The field-of-view (FOV) considered includes all voxels with sensitivity greater than or equal to 0.001 of the maximum value in the brain for either data type. The range of source–detector separations (SDS) considered is 6–60 mm. The time-window for observing the reconstructions from real data was selected as 0–11 s post-stimulus onset based on visual observation of the ROI-wise temporal mean haemodynamic response curves.

4.2.1 Simulated example case

Fig. 3 visualizes axial slices of the reconstructions for a simulated noise-free, high-contrast spherical activation corresponding to $8 \times 10^{-3}\,\mathrm{mm}^{-1}$ increase in absorption, or 40.7 μM increase in HbT. The perturbation is marked with a black line, and the slices go through the center of the sphere. The radius of the sphere was 5.5 mm limited to GM voxels. The distance from the sphere center to the surface was 12.5 mm. Fig. 3.A corresponds to the reconstruction from both FD data types, whereas Fig. 3.B is based on log-amplitude simulated measurements alone. Both cases reconstruct a lower contrast for the simulated ΔHbT, but inclusion of phase data produces approximately double the contrast. The maximum reconstructed values are 21.3 μM and 11.1 μM, for both and log-amplitude alone reconstructions, respectively, and located within the sphere. Inclusion of phase data also appears to reconstruct the shape of the simulated perturbation better, whereas in the log-amplitude case, some activity is projected towards the surface and spread.

4.2.2 Real dynamic data

Tab. 2 contains the temporal maximum (MAX), minimum (MIN) and mean (MEAN) of the spatially averaged ΔHbT time courses in the three selected ROIs introduced in Sec. 3.3. Fig. 4 visualizes the disk-wise means of the temporally-averaged ΔHbT responses along cylinders drilled from the head surface towards and (partly) through the ROIs, as visualized in Fig. 1. We note that the numbers in Tab. 2 describe the whole ROI within the FOV (which limits especially the INS-L), whereas the cylinders in Fig. 4 cover a part of the ROIs. Nevertheless, the results give many similar indications, as discussed next.

From Fig. 4 we see that the reconstructions with both FD data types show similar trends with the reconstructions from log-amplitude data alone, but inclusion of phase data appears to improve the contrast in most cases. In Tab. 2, the maximum spatially-averaged responses in the INS-L are greater when phase data is included.

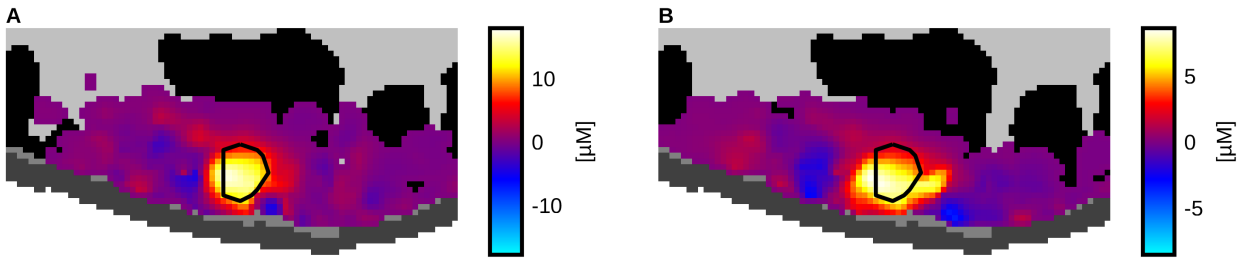

Figure 3. Axial slices of reconstructed simulated spherical absorption increase (black line) obtained with A: FD log-amplitude and phase data, and B: log-amplitude data alone. The sphere had radius of 5.5 m and ΔHbT of 40.7 μM.

Table 2. Temporal maximum (MAX), minimum (MIN) and mean (MEAN) spatially-averaged total haemoglobin concentration (HbT) changes for three regions of interest (ROI), two stimulus types (slow and fast brushing) and two data sets: FD log-amplitude and phase ($\log A$ and φ) versus log-amplitude data ($\log A$) alone.

		IFGoperc-L		
	SLOW: $\log A$ and φ	**SLOW**: $\log A$	**FAST**: $\log A$ and φ	**FAST**: $\log A$
MAX [μM]	1.4	1.9	0.6	1.1
MIN [μM]	-0.8	0.1	-1.8	-1.9
MEAN [μM]	0.1	1.3	-0.9	-0.7
		INS-L		
	SLOW: $\log A$ and φ	**SLOW**: $\log A$	**FAST**: $\log A$ and φ	**FAST**: $\log A$
MAX [μM]	0.31	0.24	0.71	0.09
MIN [μM]	-0.379	-0.002	-0.181	-0.203
MEAN [μM]	-0.06	0.11	0.19	-0.06
		PoCG-L		
	SLOW: $\log A$ and φ	**SLOW**: $\log A$	**FAST**: $\log A$ and φ	**FAST**: $\log A$
MAX [μM]	2.1	1.2	1.5	1.6
MIN [μM]	-1.2	-1.1	-0.7	0.3
MEAN [μM]	0.2	-0.2	0.6	1.1

The spatio-temporal mean ΔHbT-responses in the whole IFGoperc-L are positive for slow and negative for fast brushing, but their cylinder plots in Fig. 4A–B look relatively similar. The latter is in accordance with Pirazzoli *et al.* (2019) who found no statistically significant difference in the IFG responses to affective (hand) and non-affctive (spoon) touch in five-month-old infants.[18]

The cylinder plots for the INS-L in Fig. 4C–D show activation (= increase in HbT) for slow, and deactivation (= decrease in HbT) for fast brushing at approximate depth 10–17 mm which is somewhat more superficial than the insular cortex. This could be the insular response projected towards the head surface by the reconstruction algorithm. The projected responses would then agree with the greater response to slow versus fast brushing found in the insula by Maria *et al.* (2022).[7] In Fig. 4C, the decrease in HbT relatively deep in the head is only captured when phase data is included to the reconstruction.

For the PoCG-L, the mean responses in Tab. 2 and the cylinder plots in Fig. 4E–F show a greater response to fast versus slow brushing. The cylinder plot Fig. 4F shows a positive HbT response to fast brushing from 7 mm to 20 mm in depth; this part may be in the secondary somatosensory cortex (SII). For slow brushing, inclusion of phase data reveals a positive HbT response in the surface of the PoCG-L (SI) and negative response at depth 14–25 mm in the cylinder. Additionally, for slow brushing, the spatio-temporal mean response in the whole PoCG-L is positive when phase data is included, and negative otherwise. PoCG-L activation is expected for non-affective touch but it has also been shown in response to affective touch using fMRI.[19]

5. DISCUSSION

In this work, we introduced a method for FD DOT image reconstruction from functional neuroimaging data consisting of time courses of changes in log-amplitude and phase shift data acquired with a high-density optode arrangement. The reconstruction algorithm presented is non-iterative and utilizes the Cholesky decomposition and the Woodbury formula for efficient inversion of a very large matrix. The image reconstruction (one time instance) takes maximum 3 min for a FOV with 2.2×10^5 voxels.

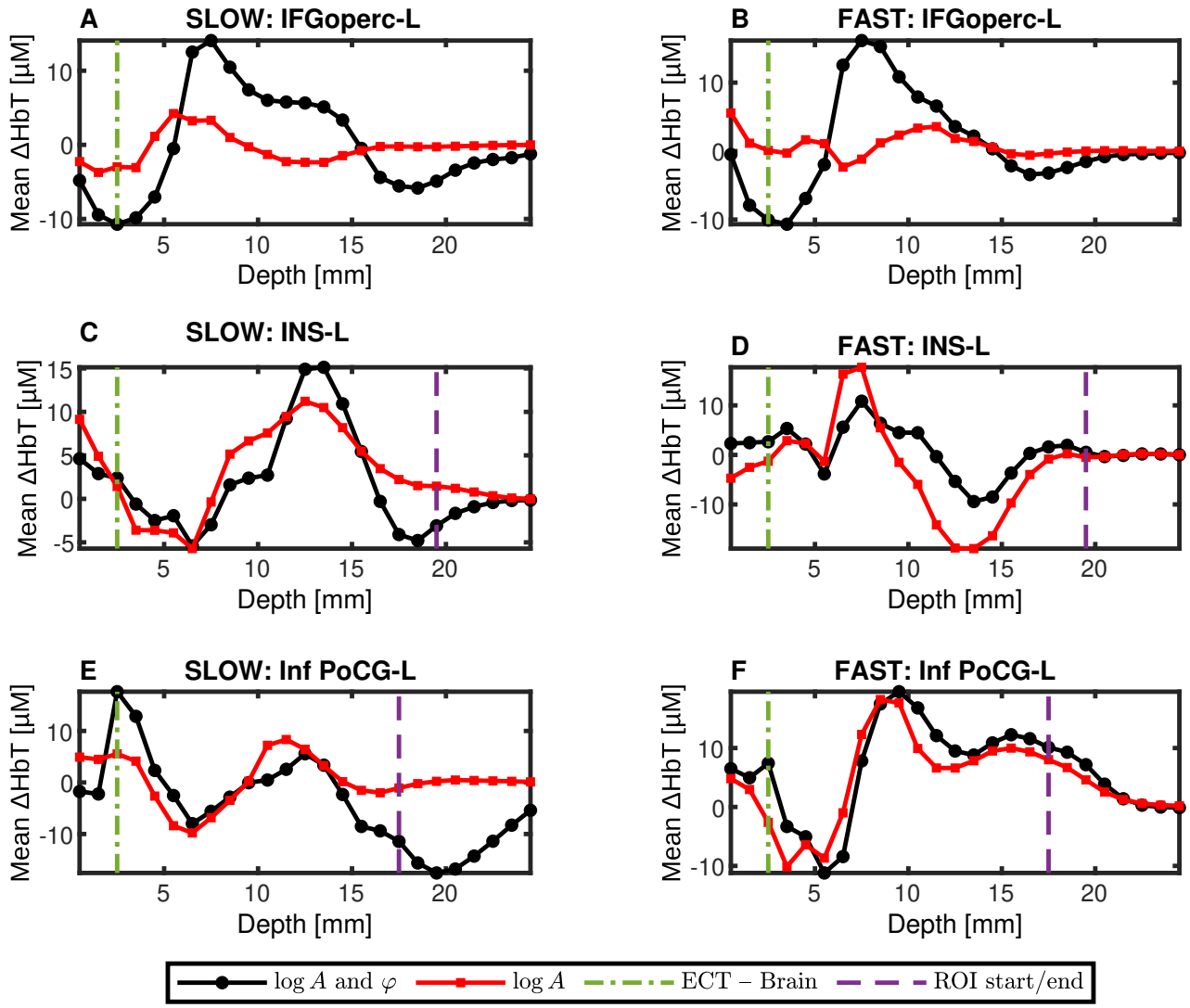

Figure 4. Time- and voxel-wise mean reconstructed changes in the total haemoglobin concentration (HbT) over the time window 0–11 s post-stimulus for slow and fast brushing over 1 mm-disk-intersections of cylinders drilled from the head surface towards three selected ROIs on the left hemisphere (See Fig. 1). The green cutted line marks the extracerebral (ECT) to brain boundary. A–B: Responses to slow and fast brushing, respectively, through the left opercular inferior frontal gyrus (IFGoperc-L). C–D: Responses to slow and fast brushing, respectively, along a cylinder that reaches the left insular cortex (INS-L) by the purple cutted line. E–F: Responses to slow and fast brushing, respectively, along a cylinder passing the inferior (Inf) end of the postcentral gyrus (PoCG-L) which ends by the purple cutted line.

Different regularization approaches could be considered in the future. For example, the Laplacian matrix could be increased to consider the 26-neighborhood instead of the 6-neighborhood. The regularization on extracerebral tissue could also be stronger to account for the peaks in sensitivity of log-amplitude for tissue voxels directly under the optodes.

All the presented simulations assumed that the detectors have a numerical aperture (NA) of 1, meaning that we did not restrict the incoming angles of the detected photons. This improves the photon detection efficiency in the simulation but reduces the accuracy of the simulation especially at short SDSs. More accurate source and detector models should be considered in the future when the methodology presented in this paper is used with measured data.

Alternative approaches to the extraction of the responses to touch could also be considered. For example, one could attempt to fit a haemodynamic response function (HRF) kernel to the time courses of real and imaginary intensity components, or the log-amplitude and phase signals. This approach can help manage the partial temporal overlap of haemodynamic responses in the data but would limit the potential to study the spatiotemporal progression of evoked haemodynamic activity. A fixed HRF model was used in Maria *et al.* 2022.[7]

The reconstructed individual-level responses to slow and fast brushing showed similarity to the population-level results by Maria *et al.* (2022)[7] and other literature. Improved signal processing, methodology and modelling can aid individual-level DOT imaging in the future.

CONCLUSIONS

In this work, we implemented new methods for utilizing frequency-domain (FD) log-amplitude and phase shift data in three-dimensional diffuse optical tomography (DOT). We added the computation of the FD sensitivity profiles, or Jacobians, to the open-source Monte Carlo eXtreme (MCX) software, and validated the outcome by comparing to the difference quotient estimates for the Jacobians and an in-house Monte Carlo code. We introduced a non-iterative image reconstruction algorithm that can efficiently handle the large inverse problems in DOT. We observed the performance of the algorithm for one two-year-old subject with simulated, and real experimental data from our previous study on slow and fast brushing processing in two-year-olds. Both simulated and real data reconstructions revealed that the inclusion of phase data can improve the image quality, in particular, by increasing the reconstructed contrast of functional changes in the brain. Reconstructed responses to slow and fast brushing in the left insular cortex and the left postcentral gyrus showed features which are generally consistent with published literature.

ACKNOWLEDGMENTS

We acknowledge the computational resources provided by the Aalto Science-IT project. Many thanks to the families participating the FinnBrain Birth Cohort Study. We also appreciate the following sources of funding: The Vilho, Yrjö and Kalle Väisälä Foundation of the Finnish Academy of Science and Letters (grant numbers 190017 and 200015 (to PH)), Academy of Finland (decisions 336788 and 336789 (to AH, NH and PH); 269282 (to IN); 273451 and 303937 (to IN); 134950 (to HK); 253270 (to HK)), Päivikki and Sakari Sohlberg Foundation (to IN), US National Institute of Health (NIH) award R01-GM114365 (to QF), Jane and Aatos Erkko Foundation (to HK and LK), Signe and Ane Gyllenberg Foundation (to HK and LK), State Research Grant (EVO) (to HK, LK and JJT), Hospital District of Southwest Finland State Research Grants (to JJT), Signe and Ane Gyllenberg Foundation (to JJT), Alfred Kordelin Foundation (to JJT), Sigrid Juselius Foundation (to JJT), Juho Vainio Foundation (to JJT), Finnish Medical Foundation (to JJT), and Emil Aaltonen Foundation (to JJT).

REFERENCES

[1] Gibson, A. P., Hebden, J. C., and Arridge, S. R., "Recent advances in diffuse optical imaging," *Physics in Medicine and Biology* **50**(4), 1–43 (2005).

[2] Nissilä, I., Noponen, T., Heino, J., Kajava, T., and Katila, T., "Diffuse optical imaging," in [*Advances in Electromagnetic Fields in Living Systems*], Lin, J. C., ed., **4**, 77–129, Springer (2005).

[3] Jönsson, E. H., Kotilahti, K., Heiskala, J., Wasling, H. B., Olausson, H., Croy, I., Mustaniemi, H., Hiltunen, P., Tuulari, J. J., Scheinin, N. M., Karlsson, L., Karlsson, H., and Nissilä, I., "Affective and non-affective touch evoke differential brain responses in 2-month-old infants," *NeuroImage* **169**, 162–171 (2018).

[4] Shekhar, S., Maria, A., Kotilahti, K., Huotilainen, M., Heiskala, J., Tuulari, J. J., Hirvi, P., Karlsson, L., Karlsson, H., and Nissilä, I., "Hemodynamic responses to emotional speech in two-month-old infants imaged using diffuse optical tomography," *Scientific Reports* **9**, 4745 (2019).

[5] Maria, A., Nissilä, I., Shekhar, S., Kotilahti, K., Tuulari, J. J., Hirvi, P., Huotilainen, M., Heiskala, J., Karlsson, L., and Karlsson, H., "Relationship between maternal pregnancy-related anxiety and infant brain responses to emotional speech–a pilot study," *Journal of Affective Disorders* **262**, 62–70 (2020).

[6] Doulgerakis, M., Eggebrecht, A. T., and Dehghani, H., "High-density functional diffuse optical tomography based on frequency-domain measurements improves image quality and spatial resolution," *Neurophotonics* **6**(3), 1–14 (2019).

[7] Maria, A., Hirvi, P., Kotilahti, K., Heiskala, J., Tuulari, J. J., Karlsson, L., Karlsson, H., and Nissilä, I., "Imaging affective and non-affective touch processing in two-year-old children," *NeuroImage* **251**, 118983 (2022).

[8] Karlsson, L., Tolvanen, M., Scheinin, N. M., Uusitupa, H.-M., Korja, R., Ekholm, E., Tuulari, J. J., Pajulo, M., Huotilainen, M., Paunio, T., and Karlsson, H., "Cohort Profile: The FinnBrain Birth Cohort Study (FinnBrain)," *International Journal of Epidemiology* **47**(1), 15–16j (2017).

[9] Nissilä, I., Noponen, T., Kotilahti, K., Katila, T., Lipiäinen, L., Tarvainen, T., Schweiger, M., and Arridge, S., "Instrumentation and calibration methods for the multichannel measurement of phase and amplitude in optical tomography," *Review of Scientific Instruments* **76**(4), 044302 (2005).

[10] Fang, Q. and Boas, D. A., "Monte Carlo simulation of photon migration in 3D turbid media accelerated by graphics processing units," *Optics Express* **17**(22), 20178–20190 (2009).

[11] Heiskala, J., Hiltunen, P., and Nissilä, I., "Significance of background optical properties, time-resolved information and optode arrangement in diffuse optical imaging of term neonates," *Physics in Medicine and Biology* **54**(3), 535–554 (2009).

[12] Heiskala, J., *Accurate modelling of tissue properties in diffuse optical imaging of the human brain*, PhD thesis, Helsinki University of Technology, Department of Biomedical Engineering and Computational Science (2009).

[13] Heiskala, J., Kotilahti, K., Lipiäinen, L., Hiltunen, P., Grant, P. E., and Nissilä, I., "Optical tomographic imaging of activation of the infant auditory cortex using perturbation Monte Carlo with anatomical a priori information," in [*Diffuse Optical Imaging in Tissue*], Pogue, B. W. and Cubeddu, R., eds., **6629**, International Society for Optics and Photonics (2007).

[14] Yao, R., Intes, X., and Fang, Q., "Direct approach to compute Jacobians for diffuse optical tomography using perturbation Monte Carlo-based photon "replay"," *Biomedical Optics Express* **9**(10), 4588–4603 (2018).

[15] Cope, M., *The Development of a Near Infrared Spectroscopy System and its Application for Non Invasive Monitoring of Cerebral Blood and Tissue Oxygenation in the Newborn Infants*, PhD thesis, University of London (1991).

[16] Hirvi, P., *Generating head models for diffuse optical tomography of the child brain*, Master's thesis, Aalto University School of Science (2019).

[17] Shi, F., Yap, P.-T., Wu, G., Jia, H., Gilmore, J. H., Lin, W., and Shen, D., "Infant Brain Atlases from Neonates to 1- and 2-Year-Olds," *PLoS ONE* **6**(4), e18746 (2011).

[18] Pirazzoli, L., Lloyd-Fox, S., Braukmann, R., Johnson, M., and Gliga, T., "Hand or spoon? Exploring the neural basis of affective touch in 5-month-old infants," *Developmental Cognitive Neuroscience* **35**, 28–35 (2019).

[19] Tuulari, J. J., Scheinin, N. M., Lehtola, S., Merisaari, H., Saunavaara, J., Parkkola, R., Sehlstedt, I., Karlsson, L., Karlsson, H., and Björnsdotter, M., "Neural correlates of gentle skin stroking in early infancy," *Developmental Cognitive Neuroscience* **35**, 36–41 (2019).